Morphological and hemodynamical alterations in brachial artery and cephalic vein. An image-based study for preoperative assessment for vascular access creation

Aristokleous, Nicolas; Houston, J. Graeme; Browne, Leonard D.; Broderick, Stephen P.; Kokkalis, Efstratios; Gandy, Stephen J.

Published in:
International Journal for Numerical Methods in Biomedical Engineering

DOI:
10.1002/cnm.3136

Publication date:
2018

Document Version
Peer reviewed version

TITLE PAGE

Title: "Morphological and Hemodynamical alterations in Brachial Artery and Cephalic Vein. An Image-Based Study for Preoperative Assessment for Vascular Access Creation"

Authors: Nicolas Aristokleous[1], J. Graeme Houston[2,3] Leonard D. Browne[1], Stephen P. Broderick[1], Efstratios Kokkalis[2], Stephen J. Gandy[4], and Michael T. Walsh[1]

Corresponding Author: Michael T. Walsh

Address: University of Limerick, V94 T9PX, Limerick, Ireland, Office L1032; Tel: +353 61202367;
email: Michael.Walsh@ul.ie

[1]*Bio-Science & Bio-Engineering Research (BioSciBER), School of Engineering, Bernal Institute and the Health Research Institute, University of Limerick, Castletroy, Limerick, Ireland*

[2]*Department of Cardiovascular and Diabetes Medicine, Ninewells Hospital and Medical School, University of Dundee, Dundee, United Kingdom*

[3]*NHS Tayside Clinical Radiology, Ninewells Hospital, Dundee, United Kingdom*

[4]*NHS Tayside Medical Physics, Ninewells Hospital, Dundee, United Kingdom*

Total number of words: 7718
Number of words of the abstract: 227
Number of figures: 7
Number of tables: 6

This article has been accepted for publication and undergone full peer review but has not been through the copyediting, typesetting, pagination and proofreading process which may lead to differences between this version and the Version of Record. Please cite this article as doi: 10.1002/cnm.3136

ABSTRACT

The current study aims to computationally evaluate the effect of right upper arm position on the geometric and hemodynamic characteristics of the brachial artery (BA) and cephalic vein (CV). Furthermore, to present in detail the methodology to characterize morphological and hemodynamical healthy vessels. Ten healthy volunteers were analyzed in two configurations, the supine (S) and the prone (P) position. Lumen 3D surface models were constructed from images acquired from a non-contrast MRI sequence. Then, the models used to numerically compute the physiological range of geometric (n=10) and hemodynamic (n=3) parameters in the BA and CV. Geometric parameters such as curvature and tortuosity, and hemodynamic parameters based on wall shear stress (WSS) metrics were calculated with the use of computational fluid dynamics. Our results highlight that changes in arm position had a greater impact on WSS metrics of the BA by altering the mean and maximum blood flow rate of the vessel. Whereas, curvature and tortuosity were found not to be significantly different between positions. Inter-variability was associated with antegrade and retrograde flow in BA, and antegrade flow in CV. Shear stress was low and oscillatory shear forces were negligible. This data suggests that deviations from this state may contribute to the risk of accelerated intimal hyperplasia of the vein in arteriovenous fistulas. Therefore, preoperative conditions coupled with post-operative longitudinal data will aid the identification of such relationships.

***Index Terms*—**Hemodialysis, Vascular access, Imaged-based computational modeling, Non-contrast MRI, Geometry

This study highlighted that changes in arm position had a greater impact on WSS metrics of the brachial artery by altering the mean and maximum blood flow rate. Whereas, curvature and tortuosity were found not to be significantly different between positions. Moreover, the image-based CFD analysis highlighted an inter-variability of shear stress metrics within a small sample of healthy subjects which lead to the postulation that deviations from homeostatic conditions will modulate remodelling rather than exceeding a global threshold.

INTRODUCTION (700)

A native arteriovenous fistula (AVF) is the preferred access route for end stage renal disease (ESRD) patients undergoing hemodialysis [1,2]. According to the guidelines of the National Kidney Foundation the site order for the surgical intervention of AVF for hemodialysis (HD) is the following: forearm (radio–cephalic or distal AVF), elbow (brachio–cephalic or proximal AVF), arm (brachial–basilic AVF with transposition or proximal AVF) [3]. The brachio–cephalic fistula has the advantage of employing major caliber autologous material, which facilitates both the making up of the access and the subsequent venous cannulation for the use of access, as well as a higher patency rate compared with distal ones, but comes at a price of a higher rate of complications such as steal syndrome and arterial alterations in cardiac output [3]. Improved patency and lower infection rates are obtained compared to grafts and catheters. However, AVF primary patency rates are poor ranging from 44-60% [4,5] due to inadequate dilation and stenosis at the access site [6].

AVF creation offers a unique model of vascular adaption, it involves the direct anastomosis of an artery to a vein and results in immediate changes to both geometry and flow. It is widely perceived that the change in local hemodynamics beyond their normal physiological range stimulates remodelling in both the arterial and venous vasculature. This

remodelling aims to normalise forces towards homeostatic conditions [7]. The coupling between geometry and flow and the subsequent alteration of these parameters over time may shift areas within these vessels to an unfavourable state during the remodelling process. The precise conditions under which intimal hyperplasia (IH) and lumen loss are aggressively promoted during remodelling remains unclear. Despite this, a consensus is emerging that low or subnormal shear stress may induce severe stenotic lesions due to intimal thickening [8,9]. Some studies even rely on this theory for the assessment and optimisation of anastomotic configurations to aid surgical practice [10].

Previous studies in healthy adults have shown notable changes in geometry and hemodynamics in large peripheral and head arteries with posture change. More specifically, Glor *et al.* have first reported that head rotation may cause geometric changes to the right carotid bifurcation with leftward rotation of the head [11]. Then, other researchers cited alterations due to posture changes to the popliteal artery [12], vertebral arteries [13], right and left carotid bifurcation [14]. The objective of this study was therefore to present a methodology to calculate geometric and hemodynamic parameters in healthy arm vessels, and to find their range of variation in two investigated positions. These postures are the normal supine similarly taking place during the hemodialysis session and the prone with the arm outstretched above the head, as an extreme posture to point out the outlier alterations. For MRI examinations of the arm, the described prone orientation is preferable since it is possible to maintain the anatomical area of interest centrally within the homogeneous region of the scanner magnetic field. However patient compliance is generally better when the anatomical area of interest is scanned in the supine orientation - albeit at the expense of certain image quality features such as signal-to-noise and homogeneity.

It has been shown that the patient-based preoperative geometric and hemodynamic characteristics of the circulatory system with the use of computational fluid dynamics (CFD) can assist the physician during the treatment planning [15,16]. In this paper we initiate a study to ascertain the homeostatic shear level of the brachial artery (BA) and cephalic vein (CV). These vessels are commonly utilised and manipulated to some degree to form a fistula in the upper arm. Although a growing body of evidence exists describing the hemodynamic environment within AVFs, little to no data is available that defines the preoperative or homeostatic environment of brachial arteries and cephalic veins in relation to geometry and flow. It is postulated that preoperative flow conditions may impact maturation when an AVF is created and provide insight into the statistical variations in AVF patency observed in clinical practice. Identifying a deviation from the normal hemodynamic state, preoperatively, may be an additional factor which will contribute to AVF non-maturation and failure.

MATERIALS AND METHODS

A. Study Group

The group of ten subjects (n=10) for the morphology studies consisted of six and four asymptomatic, male/female volunteers (mean age of 32 and 33 years, range from 28-45 and 27-44 years, respectively). For the flow studies a subgroup of three subjects (n=3) was selected. Each subject was imaged in two different scanning sessions corresponding to the two investigated arm postures: 1) the supine arm position (S) and 2) the prone position with the arm outstretched above the head (P). The study was approved by the NHS Scotland Research Ethics Service (2014).

B. MR Imaging

MR images were obtained with a 3T MR unit (MAGNETOM Trio MR, Siemens, Germany) using a surface coil (8 Channel, Siemens) which was wrapped around the participant's arm of interest to enable signal detection. A gradient echo sequence was used for initial anatomical localization, and this was followed by the application of a high spatial resolution MEDIC (Multi-Echo Data Image Combination) MR imaging sequence with fat suppression. The sequence was optimised with the following acquisition parameters as outlined in Table 1. A 2D phase contrast sequence (PCMRI) was used for velocity encoding (VENC) of the arterial and venous segments, with parameters outlined in Table 1. Scans were firstly acquired in the supine position with the participant's right arm relaxed and extended by their side, and then repeated in the prone position with their arm extended above their head Figure 1(a).

C. Surface reconstruction and geometric quantification

For each participant, semi-automated segmentation of the 3D MEDIC data was performed with Amira (FEI, Visualization Sciences Group, France and Zuse Institute Berlin, Germany) to obtain a 3D isosurface of the intra-luminal volume of the vessels. A grey-scale value threshold with manual adaption was combined to acquire the 3D lumen. The remeshed surfaces were imported into Blender 3D (Blender.org) and were truncated a set distance of 60 mm from the confluence of the basilic vein and were extended distally and truncated before the next branch or vessel confluence. Meshlab (1.3.3, Visual Computing Lab, ISTI, Italy) was used to smooth the segmented surface data. A Taubin filter and a Laplacian surface preservation filter were applied to remove high curvature variations and smooth the surface without producing shrinkage. The vascular modelling toolkit (VMTK) was utilised to generate centrelines and corresponding geometrical data of the vessels [17].

The reproducibility of geometric reconstruction and the accuracy of the segmentation and reconstruction procedures was assessed with repetition of segmentation, smoothing and geometric characterization steps, for Case 1, for both investigated arm positions, by two users. The percentage difference in the calculations of the geometric parameters was found to be below 5%, which is acceptable (more details can be found in [18]).

D. Computational Simulations

The image-based computational modeling methodology employed in the present work, from MR images to CFD simulations [13,19] allows estimating hemodynamic parameters based on wall shear stress (WSS) metrics, which have been found to be important in the development of thrombosis arising from intimal hyperplasia [20]. The accuracy of CFD predictions investigated by Steinman *et al.* and concluded that the pressure drop was reasonable well predicted [21].

Blood flow time history was obtained by integrating the through-plane velocity over the lumen cross-sectional area at each cardiac phase using Segment (Medviso, Sweden) [22]. All semi-automated segmentation and flow segmentation was undertaken by the same user to eliminate operator inter-variability.

The unsteady 3D incompressible Navier-Stokes equations were solved using a commercial CFD code (Star CCM+, CD-Adapco, USA). The discretisation scheme was second order in both space and time. A transient time step of 1ms was used and the flow was solved over four cycles, with the first cycle eliminated from the results analysis. Rigid boundaries and the no-slip condition were enforced at walls. Blood was modelled as an incompressible Newtonian fluid with a density of 1050 kg/m3 and a dynamic viscosity of 0.0035 kg/m·s. Time-dependent boundary conditions were prescribed at the arterial and venous inlets. Traction-free boundary conditions were applied at the outlet. A fully developed velocity profile was applied at the brachial artery inlet, whereas a flat profile was employed

for the cephalic vein. The assumption of Newtonian rheology and rigid walls was considered reasonable since these assumptions have been widely used in previous CFD studies [23–25].

A structured hexahedral mesh was created with a mean of $0.595x10^6$ and $0.730x10^6$ elements employed for the artery and vein cases respectively. Hexahedral meshes are preferred to tetrahedral or prismatic as they require less number of elements for a fixed level of accuracy. Specifically, as it was shown by De Santis *et al.* [26], the same accuracy can be achieved with six times fewer hexahedral elements compared to tetrahedral or prismatic meshes, and that hexahedral elements based simulations converged much faster requiring 14 times less CPU hours. The impact of these assumptions in hemodynamic simulations has been discussed extensively in [27,28]. A grid convergence study has to be conducted for each model to ensure grid and time step convergence. Since, however, topology and flow features in all presented cases are expected to be roughly similar we conducted a study on a single case, and acquired results were applied to all cases. The grid convergence was determined as outlined per standards of the Journal of Fluids Engineering [29]. Simulations using steady inflow boundary conditions were conducted for a blood flow rate of 456 ml/min corresponding to values near systolic peak for the pulsatile analysis of case 2. Successive meshes with a refinement factor greater than 1.5 were used; these meshes consisted of 176064, 595840 and 1997458 hexahedral elements respectively. WSS is a critical quantity with respect to grid convergence. Therefore, time-averaged WSS (TAWSS) magnitude was chosen as term of comparison of the grids. It was analysed by using the surface averaged value over an integration time of 3 seconds. The numerical uncertainty in the fine gird solution for surface averaged of the TAWSS is reported as 0.01%. Table 2 quantifies the relative error and grid convergence index (GCI).

E. Post processing

A range of shear stress metrics outlined in Table 3 were extracted from the vascular surface. The TAWSS is calculated by integrating the WSS vector at each nodal point over the cardiac cycle. The cycle averaged wall shear stress gradient (TAWSSG) measures the spatial change in TAWSS over the cardiac cycle, the temporal wall shear stress gradient (TWSSG) which quantifies the rate of change of the shear stress vector was calculated and averaged over the cycle [30–32]. Directional changes in shear stress were quantified with the oscillating shear index (OSI) and Transverse WSS (TransWSS) [33,34]. The relative residence time (RRT) which indicates the residence time of particles near the vessel wall was also extracted [35]. Bulk flow features were assessed using a helicity based descriptor. The kinetic helicity density (Hk), is a measure of the alignment of the velocity vector (v) and the vorticity vector (ω). Both instantaneous and time averaged values were determined. Normalising Hk, with the velocity and vorticity magnitude results in a measure referred to as the Local Normalised Helicity (LNH) [36]. The LNH is a useful quantity to visualise complex flow patterns such as helical flow [37].

Each vessel was segmented from its inlet at 20 mm intervals along the curvilinear abscissa of its centreline. Surface averages of shear stress parameters were taken for each interval. For each segment, curvature (k) at each point, aggregated curvature (AC) and tortuosity defined in equations (1) and (2) were determined to compare positional changes. Where L is an approximation of the curve length and D is the distance between its two end points of the segment.

$$AC = \left(\sum_{i=1}^{n} |k|\right)/n \tag{1}$$

$$Tortuosity = \left(\frac{L}{D}\right) - 1 \quad (2)$$

F. Statistical analysis

Geometric data is presented as mean with standard deviation to assess the variation amongst the cases. The Wilcox rank sum test was utilised to assess the difference of geometric features between the supine and prone positions with significance established with a $p < 0.05$.

RESULTS

All MR images were acquired successfully, although in some cases physical compression on the vessel was noted to prevent venous filling on the flow images when the patient was in the prone position. For this reason, only the supine position was considered for analysis of the cephalic vein.

A. Flow Data

The brachial artery waveforms of cases 1 and 2 exhibited antegrade flow in both supine and prone positions, whereas case 3 was retrograde in both. Figs. 2a, 3a and 4a show qualitatively the significant reduction in both mean and peak blood flow rates due to prone position and the quantitative results indicating the constant decrease ~50% are detailed in Table 4. The most notable change occurred in case 2 where the prone position significantly reduced the mean flow rate and the waveform changed from a high acceleration monophasic profile to low acceleration monophasic profile. The venous waveform had a monophasic profile with a low acceleration.

B. Geometric analysis

There was no significant difference between the curvature and tortuosity of the brachial artery between supine and prone positions for all cases (n=10), as illustrated in Table 5. For cases 1, 2 and 3, it is clear from Figure 2, 3 and 4 that the proximal artery curves or arcs as it traverses distally toward the elbow. The cephalic vein follows a similar trend but in the opposite direction curving distally to proximally as highlighted in Figure 5.

C. Bulk flow descriptors

The Localised normalised helicity (LNH) within the brachial arteries was low. For cases 1 and 2 in which the flow was antegrade, the bulk flow contained counter rotating vortical structures of low magnitude. However, a prominent right handed helical structure was evident within the fluid domain in the supine position for these cases. For the prone position, bi-helical patterns characterised the flow field and vortical structures occupied a relatively small portion of the domain, there was no dominant rotation direction. For case 3, in which there is retrograde flow, there was no dominant rotational direction and low magnitude bi-helical patterns characterised the flow field for both the supine and prone positions. For the venous cases, inter-individual variations can also be noticed. Visualisation of the Isosurfaces of LNH (± 0.1) revealed that helical flow was weak as low magnitude bi-directional vortical structures characterised the bulk flow.

D. Shear stress metrics

Brachial Artery: For case 1 and 2, TAWSS ranged from 1.01-2.85 Pa in the supine position and from 0.78-1.38 Pa in the prone position as shown in Table 6. TAWSS is reduced in the prone position due to the reduction in mean and peak flow rates in all cases, resulting in lower TAWSSG, TransWSS and Temporal gradients compared to the supine position. TAWSSG, TransWSS and Temporal gradients ranged from 160.82-601.23 Pa/m, 0.03-0.09 Pa and 356.01-642.28 Pa/s in the supine position compared to 47.70-306.94 Pa/m, 0.01 to

0.03 Pa and 84.05-407.11Pa/s in the prone. OSI values were low and occupied a small area of the inner curvature of the brachial artery segments in these cases as illustrated in Figure 6, resulting in a low range of 0.01-0.03 in both positions.

For case 3, retrograde flow lead to a lower level of TAWSS within the brachial artery, which ranged from 0.38-0.44 Pa and from 0.20-0.31 Pa for the supine and prone positions (Table 6). Higher levels of flow reversal were recorded in the prone position as a larger volume of flow was reversed compared to the supine position as illustrated in Figure 4(a). This is reflected by high levels in the range of TAWSSG, OSI, TransWSS and RRT (71.36-329.59 Pa/m, 0.26-0.28, 0.01-0.16 Pa and 3.65-4.68) in the prone compared to the supine position respectively (104.92-144.83 Pa/m, 0.12-0.22, 0.03 to 0.14 Pa, 1.77-2.46). Negative temporal gradients arise due directional change.

Cephalic vein: For the cephalic vein, flow was antegrade in all cases. However, the range of TAWSS, TAWSSG and temporal gradients varied from case to case (Figure 7). The differences were attributable to differences in flow rate and cross sectional area of the vessels. The difference in cross sectional shape was most notable in case 2 as the vessels elliptical shape tapers in segments 2 and 3 increasing TAWSS, TAWSSG and temporal gradients. TAWSS, TAWSSG and temporal gradients ranged from 0.09-0.14 Pa, 9.10-34.64 Pa/m and 3.06-4.43 Pa/s in case 1. These metrics ranged 0.68-0.75 Pa, 62.73-268.11 Pa/m and -99.17 to -60.71 Pa/s respectively in case 2. Finally in case 3, these metrics ranged from 0.24-0.39 Pa, 0.24–0.39 Pa, 27.32-136.79 Pa/m and -125.93 to -78.85 Pa/s. The negative temporal gradients were associated with a longer or steeper deceleration phase of the flow waveforms as illustrated in Figure 5. In all cases, measures of OSI and TransWSS were negligible.

DISCUSSION

This study has highlighted that the brachial artery and cephalic vein of the right upper arm exhibit inter-variability in terms of the range of shear stress metrics the endothelium is exposed to at rest in healthy subjects. The change in arm position had a greater impact on shear stress metrics of the brachial artery by altering the mean and maximum flow rate of the vessel rather than altering its curvature or tortuosity.

The deviations in flow rate lead to a variation in the level of TAWSS, TAWSSG and temporal gradients of the brachial artery. The retrograde flow of case 3 lead to a lower range of TAWSS, TAWSSG and temporal gradients in both supine and prone positions. Flow reversal augmented levels of OSI and TransWSS in this brachial artery compared to the previous cases for which low magnitudes of OSI and TransWSS were only found to occupy the inner curvature of the vessel. The appearance of the retrograde flow is striking if focus is placed on the pattern of OSI. However, the shape of the venous waveform in this subject is sinusoidal and is similar in magnitude to the other participants. Although, the curvature and tortuosity of this vessel is similar to the other two participants and the cross sectional shape is less elliptical and more circular. To the best of our knowledge, this difference is not pathological and is within the normal range of healthy volunteers as all participants were free from cardiovascular disease and diabetes. Moreover, they had no history of diabetes or hypertension, hyperlipidemia, or malignancy which are traditional risk factors associated with Chronic kidney disease (CKD) and CKD progression to ESRD. Therefore, we deemed the study population to be representative of a healthy population in the context of CKD.

It is interesting to note, that the level of TAWSS in case 3 is below the 0.5 Pa threshold which is cited as stimulating intimal thickening [8]. Either this vascular segment is in a process of re-equilibration toward a global shear stress value or the vessel is in a stable physiological state. As the subject was at rest, with no external compression of the upper arm

it is difficult to debate that the acquisition is not the baseline or physiological condition of the vessel. This vessel is also exposed to high levels of reversed flow and oscillating forces which are often cited as risk factors of atherosclerosis [38–40].

The quiescent level of shear stress within a vascular segment is dependent on its location, cross sectional shape, curvature, tortuosity and branching. Coupled with the inter-variability of flow rate, blood pressure and vessel compliance within a population it is unlikely that 'a one fits all' threshold based on absolute high or low magnitudes of shear stress initiates responsive vascular remodelling. Rather, one would conjecture that deviations in the level of shear stress from its quiescent state would initiate vascular remodelling to return the vessel to its homeostatic state.

A high amount of helicity has been shown to suppress flow disturbances within vasculature segments such as bifurcations, anastomoses and the aortic arch. This effect is believed to be moderated when one direction of rotation dominates [41]. For the antegrade cases a prominent right handed vortical structure emerged. This would suggest that the underlying brachial artery geometry contributes to the onset and development of helical flow with a dominant direction of rotation. However, the helical content of the vessels is remarkably low and deviations in position easily disrupted the bulk flow leading to bi-helical structures and a loss of a dominant rotating structure. For the retrograde case, the bulk flow is characterised by weak and low magnitude bi-helical structures in both positions.

The helical content of the cephalic vein was also characterised by weak incoherent bi-helical structures. Analysing the helical content of arterial flow as a diagnostic strategy to identify regions of disturbed flow and areas at risk of developing atherosclerotic lesions may be less robust and applicable than previously taught as low and bi-helical structures were found at rest in this healthy cohort. Whether, its efficacy is more suited to bifurcations and

anastomoses where deviations to aberrant changes in geometry and flow are more prominent requires further investigation.

The prone position compressed the cephalic vein restricting flow, which prevented a complete analysis of positional change in this study. The cross-sectional shape of the cephalic vein is more elliptical in shape than that of arteries. This variation in cross sectional shape in conjunction with varying flow rates contributed to the varying range of shear stress metrics reported in this analysis. As the flow rate is significantly reduced compared to that of the brachial artery it was expected that TAWSS, TAWSSG and temporal gradients would be lower (Table 6). The waveform of the cephalic vein is sinusoidal in shape and can be attributed to elastic recoil associated with filling pressure and involuntary contraction of surrounding muscles. The absence of oscillatory shear forces in this analysis would suggest the venous endothelium is not commonly exposed to oscillating forces except at confluences and behind venous valves [42].

Both the brachial artery and cephalic vein are commonly manipulated and utilised for AVF creation. The anatomically localised patterns of aggressive intimal hyperplasia and stenosis within AVFs are predominately found to occur in the swing segment, which is the segment of the vein immediately downstream of the anastomosis [43]. This section can be highly curved and tortuous and can exhibit regions of oscillatory flow with large spatial and temporal gradients of shear stress which represent an abnormal deviation from the vessels physiological state [7,24,44]. The exposure of the venous endothelium to enhanced flow and shear stress is known to modulate an arterialisation of the vein [45,46]. Whether, regions exposed to levels of TAWSS below the subnormal arterial range or subnormal venous range modulate intimal thickening in this configuration has yet to be made clear.

Limitations: We acknowledge the small sample size of this study as a limitation. Larger sample sizes are needed to observe further hemodynamic and geometric trends and variability of population. Additionally, the age range of the selected volunteers (27-45) is also a limitation since direct observations may not be attributable to those candidates for AVF creation who are usually older. We chose to study younger individuals as they were better able to tolerate the more uncomfortable prone position (with the arm outstretched above the head) for the full duration of the scan within the MRI scanner.

We acknowledge that the assumption of rigid walls for both the artery and vein is a major limitation of the numerical simulations presented, particularly for the venous segments which are known to be highly elastic and deformable. This oscillatory wall motion can have a notable effect on shear stress distribution. The non-contrast imaging technique utilised in this analysis relies on inflow effects and is dependent on blood flow velocities. The variations in blood flow velocities and asymmetry of vessels lead to spatial variations in image quality and intensity.

CONCLUSIONS

This preliminary study shows that non-contrast MRI-based CFD can be utilised to noninvasively analyse geometric and hemodynamic parameters within upper arm vessels – sites commonly used for venous access creation. Here, we have presented a methodology to characterize the morphology and the hemodynamical field within large healthy vessels. This analysis highlighted that there is an inter-variability of shear stress metrics within a small sample of healthy subjects at rest which lead to the postulation that deviations from homeostatic conditions will modulate remodelling rather than exceeding a global threshold. Kroll *et al.* and Van Tricht *et al.* reported the normal WSS values, for large veins to be in the range of 0.076 to 0.76 Pa [47,48]. Here, the global threshold hypotheses for veins appear to remain valid as our data from Figure 7 indicates that the results fall in this range – except for the single value of 0.85 Pa.

MR image acquisition in the supine position is recommended to provide quantifiable measures of upper arm vessels. Altering hand/arm position had no significant effect on curvature and tortuosity of the brachial artery, but positional change was found to notably alter the mean and peak blood flow rate and subsequent levels of shear metrics within the artery. Unsteady flow was documented in the cephalic vein and oscillatory shear forces were found to be negligible in this analysis. The current paradigm that intimal hyperplasia is induced by a low threshold of TAWSS fails to provide a mechanistic understanding of why severe stenotic lesions occur in the venous segments of AVFs especially as these levels are found to occur at rest in healthy subjects. Whether, deviations from its physiological state such as persistent flow reversal modulates aggressive intimal hyperplasia and lumen loss of the vein requires further investigation.

ACNOWLEDGEMENTS

This work was co-funded by European Union's Seventh Framework Programme for research, technological development and demonstration (grant agreement no: 324487, ReDVA) and Science Foundation Ireland (SFI Career Development Award 15/CDA/3323).

Conflict of interest statement

The authors have no conflict of interest related to this study.

References

1. Shenoy S. Innovative surgical approaches to maximize arteriovenous fistula creation. *Seminars in vascular surgery* 2007; **20**(3): 141–7. DOI: 10.1053/j.semvascsurg.2007.07.005.

2. Tordoir J, Canaud B, Haage P, *et al.* EBPG on vascular access. *Nephrology Dialysis Transplantation* 2007; **22**(SUPPL.2). DOI: 10.1093/ndt/gfm021.

3. Santoro D, Benedetto F, Mondello P, *et al.* Vascular access for hemodialysis: Current perspectives. *International Journal of Nephrology and Renovascular Disease* 2014; **7**: 281–294. DOI: 10.2147/IJNRD.S46643.

4. Tordoir JHM, Rooyens P, Dammers R, van der Sande FM, de Haan M, Yo TI. Prospective evaluation of failure modes in autogenous radiocephalic wrist access for haemodialysis. *Nephrology, dialysis, transplantation : official publication of the European Dialysis and Transplant Association - European Renal Association* 2003; **18**(2): 378–83.

5. Lee T, Barker J, Allon M. Comparison of survival of upper arm arteriovenous fistulas and grafts after failed forearm fistula. *Journal of the American Society of Nephrology* 2007; **18**(6): 1936–41. DOI: 10.1681/ASN.2006101119.

6. Rothuizen TC, Wong C, Quax PHA, Van Zonneveld AJ, Rabelink TJ, Rotmans JI. Arteriovenous access failure: More than just intimal hyperplasia? *Nephrology Dialysis Transplantation* 2013; **28**(5): 1085–1092. DOI: 10.1093/ndt/gft068.

7. McGah PM, Leotta DF, Beach KW, Eugene Zierler R, Aliseda A. Incomplete Restoration

of Homeostatic Shear Stress Within Arteriovenous Fistulae. *Journal of Biomechanical Engineering* 2012; **135**(1): 11005. DOI: 10.1115/1.4023133.

8. Sho E, Nanjo H, Sho M, *et al.* Arterial enlargement, tortuosity, and intimal thickening in response to sequential exposure to high and low wall shear stress. *Journal of Vascular Surgery* 2004; **39**(3): 601–612. DOI: 10.1016/j.jvs.2003.10.058.

9. Sho M, Sho E, Singh TM, *et al.* Subnormal shear stress-induced intimal thickening requires medial smooth muscle cell proliferation and migration. *Experimental and Molecular Pathology* 2002; **72**(2): 150–160. DOI: 10.1006/exmp.2002.2426.

10. Ene-Iordache B, Cattaneo L, Dubini G, Remuzzi A. Effect of anastomosis angle on the localization of disturbed flow in "side-to-end" fistulae for haemodialysis access. *Nephrology Dialysis Transplantation* 2013; **28**(4): 997–1005. DOI: 10.1093/ndt/gfs298.

11. Glor FP, Ariff B, Hughes a D, *et al.* Influence of head position on carotid hemodynamics in young adults. *Am. J. Physiol. Heart Circ. Physiol.* 2004; **287**(4): H1670-81. DOI: 10.1152/ajpheart.01186.2003.

12. Conti M, Marconi M, Campanile G, *et al.* Patient-specific finite element analysis of popliteal stenting. *Meccanica* 2017; **52**(3): 633–644. DOI: 10.1007/s11012-016-0452-9.

13. Aristokleous N, Seimenis I, Georgiou GC, Nicolaides A, Anayiotos AS. The Effect of Head Rotation on the Geometry and Hemodynamics of Healthy Vertebral Arteries. *Annals of Biomedical Engineering* 2015; **43**(6): 1287–1297. DOI: 10.1007/s10439-015-1340-5.

14. Papaharilaou Y, Aristokleous N, Seimenis I, *et al.* Effect of head posture on the healthy human carotid bifurcation hemodynamics. *Medical and Biological Engineering and Computing* 2013; **51**(1–2). DOI: 10.1007/s11517-012-0985-6.

15. Merkx MAG, Bode AS, Huberts W, *et al.* Assisting vascular access surgery planning for hemodialysis by using MR, image segmentation techniques, and computer simulations. *Medical & Biological Engineering & Computing* 2013; **51**(8): 879–889. DOI:

10.1007/s11517-013-1060-7.

16. Taylor CA, Draney MT, Ku JP, *et al.* Predictive Medicine: Computational Techniques in Therapeutic Decision-Making. *Computer Aided Surgery* 1999; **4**(5): 231–247. DOI: 10.3109/10929089909148176.

17. Antiga L, Steinman DA. Robust and Objective Decomposition and Mapping of Bifurcating Vessels. 2004; **23**(6): 704–713.

18. Aristokleous N, Seimenis I, Papaharilaou Y, *et al.* Effect of posture change on the geometric features of the healthy carotid bifurcation. *IEEE Transactions on Information Technology in Biomedicine* 2011; **15**(1): 148–154. DOI: 10.1109/TITB.2010.2091417.

19. Berg P, Roloff C, Beuing O, *et al.* The Computational Fluid Dynamics Rupture Challenge 2013 - Phase II: Variability of Hemodynamic Simulations in Two Intracranial Aneurysms. *Journal of Biomechanical Engineering* 2015; **137**(12). DOI: 10.1115/1.4031794.

20. Browne LD, Bashar K, Griffin P, Kavanagh EG, Walsh SR, Walsh MT. The role of shear stress in arteriovenous fistula maturation and failure: A systematic review. *PLoS ONE* 2015; **10**(12): 1–24. DOI: 10.1371/journal.pone.0145795.

21. Steinman D a, Hoi Y, Fahy P, *et al.* Variability of computational fluid dynamics solutions for pressure and flow in a giant aneurysm: the ASME 2012 Summer Bioengineering Conference CFD Challenge. *Journal of biomechanical engineering* 2013; **135**(2): 21016.

22. Heiberg E, Sjögren J, Ugander M, Carlsson M, Engblom H, Arheden H. Design and validation of Segment--freely available software for cardiovascular image analysis. *BMC medical imaging* 2010; **10**: 1. DOI: 10.1186/1471-2342-10-1.

23. Browne LD, Griffin P, Bashar K, Walsh SR, Kavanagh EG, Walsh MT. In Vivo Validation of the In Silico Predicted Pressure Drop Across an Arteriovenous Fistula. *Annals of Biomedical Engineering* 2015; **43**(6): 1275–1286. DOI: 10.1007/s10439-015-1295-6.

24. Botti L, Van Canneyt K, Kaminsky R, *et al.* Numerical Evaluation and Experimental

Validation of Pressure Drops Across a Patient-Specific Model of Vascular Access for Hemodialysis. *Cardiovascular Engineering and Technology* 2013; **4**(4): 485–499. DOI: 10.1007/s13239-013-0162-6.

25. McGah PM, Leotta DF, Beach KW, Aliseda A. Effects of wall distensibility in hemodynamic simulations of an arteriovenous fistula. *Biomechanics and Modeling in Mechanobiology* 2014; **13**(3): 679–695. DOI: 10.1007/s10237-013-0527-7.

26. De Santis G, Mortier P, De Beule M, Segers P, Verdonck P, Verhegghe B. Patient-specific Computational Fluid Dynamics: Structured mesh generation from coronary angiography. *Medical and Biological Engineering and Computing* 2010; **48**(4): 371–380. DOI: 10.1007/s11517-010-0583-4.

27. Morbiducci U, Gallo D, Massai D, *et al.* Outflow conditions for image-based hemodynamic models of the carotid bifurcation: implications for indicators of abnormal flow. *Journal of biomechanical engineering* 2010; **132**(9): 91005. DOI: 10.1115/1.4001886.

28. Moyle KR, Steinman DA. Inlet Conditions for Image-Based CFD Models of the Carotid Bifurcation : Is it Reasonable to Assume Fully Developed Flow ? 2006; **128**(June): 371–379. DOI: 10.1115/1.2187035.

29. Celik IB, Ghia U, Roache PJ, Freitas CJ, Coleman H, Raad PE. Procedure for Estimation and Reporting of Uncertainty Due to Discretization in CFD Applications. *Journal of Fluids Engineering* 2008; **130**(7): 78001. DOI: 10.1115/1.2960953.

30. Browne LD, O'Callaghan S, Hoey DA, Griffin P, McGloughlin TM, Walsh MT. Correlation of Hemodynamic Parameters to Endothelial Cell Proliferation in an End to Side Anastomosis. *Cardiovascular Engineering and Technology* 2014; **5**(1): 110–118. DOI: 10.1007/s13239-013-0172-4.

31. Ojha M. Spatial and temporal variations of wall shear stress within an end-to-side arterial anastomosis model. *Journal of Biomechanics* 1993; **26**(12). DOI: 10.1016/0021-

9290(93)90089-W.

32. Lei M, Archie JP, Kleinstreuer C. Computational design of a bypass graft that minimizes wall shear stress gradients in the region of the distal anastomosis. *Journal of Vascular Surgery* 1997; **25**(4): 637–646. DOI: 10.1016/S0741-5214(97)70289-1.

33. He X, Ku DN. Pulsatile flow in the human left coronary artery bifurcation: average conditions. *Journal of biomechanical engineering* 1996; **118**(1): 74–82. DOI: 10.1115/1.2795948.

34. Peiffer V, Sherwin SJ, Weinberg PD. Computation in the rabbit aorta of a new metric - the transverse wall shear stress - to quantify the multidirectional character of disturbed blood flow. *Journal of Biomechanics* 2013; **46**(15): 2651–2658. DOI: 10.1016/j.jbiomech.2013.08.003.

35. Lee S-W, Antiga L, Steinman DA. Correlations among indicators of disturbed flow at the normal carotid bifurcation. *Journal of biomechanical engineering* 2009; **131**(6): 61013. DOI: 10.1115/1.3127252.

36. Morbiducci U, Ponzini R, Rizzo G, *et al.* Mechanistic insight into the physiological relevance of helical blood flow in the human aorta: An in vivo study. *Biomechanics and Modeling in Mechanobiology* 2011; **10**(3): 339–355. DOI: 10.1007/s10237-010-0238-2.

37. Morbiducci U, Diego G, Ponzini R, *et al.* Quantitative analysis of bulk flow in image-based hemodynamic models of the carotid bifurcation: The influence of outflow conditions as test case. *Annals of Biomedical Engineering* 2010; **38**(12): 3688–3705. DOI: 10.1007/s10439-010-0102-7.

38. Tarbell JM, Shi Z-D, Dunn J, Jo H. Fluid Mechanics, Arterial Disease, and Gene Expression. *Annual Review of Fluid Mechanics* 2014; **46**(1): 591–614. DOI: 10.1146/annurev-fluid-010313-141309.

39. Cunningham KS, Gotlieb AI. The role of shear stress in the pathogenesis of

atherosclerosis. *Laboratory Investigation* 2004; **85**(1): 9–23. DOI: 10.1038/labinvest.3700215.

40. Aristokleous N, Seimenis I, Georgiou GC, *et al.* Impact of head rotation on the individualized common carotid flow and carotid bifurcation hemodynamics. *IEEE Journal of Biomedical and Health Informatics* 2014; **18**(3): 783–789. DOI: 10.1109/JBHI.2014.2305575.

41. Gallo D, Steinman DA, Bijari PB, Morbiducci U. Helical flow in carotid bifurcation as surrogate marker of exposure to disturbed shear. *Journal of Biomechanics* 2012; **45**(14): 2398–2404. DOI: 10.1016/j.jbiomech.2012.07.007.

42. Chiu J-J, Chien S. Effects of dsisturbed flow on vascular endothelium : pathophysiological basis and clinical perspectives. *Physiol Rev* 2011; **91**(1): 327–387. DOI: 10.1152/physrev.00047.2009.

43. Badero OJ, Salifu MO, Wasse H, Work J. Frequency of Swing-Segment Stenosis in Referred Dialysis Patients With Angiographically Documented Lesions. *American Journal of Kidney Diseases* 2008; **51**(1): 93–98. DOI: 10.1053/j.ajkd.2007.09.012.

44. He Y, Terry CM, Nguyen C, Berceli SA, Shiu YTE, Cheung AK. Serial analysis of lumen geometry and hemodynamics in human arteriovenous fistula for hemodialysis using magnetic resonance imaging and computational fluid dynamics. *Journal of Biomechanics* 2013; **46**(1): 165–169. DOI: 10.1016/j.jbiomech.2012.09.005.

45. Ravani P, Brunori G, Mandolfo S, *et al.* Cardiovascular Comorbidity and Late Referral Impact Arteriovenous Fistula Survival: A Prospective Multicenter Study. *Journal of the American Society of Nephrology* 2004; **15**(1): 204–209. DOI: 10.1097/01.ASN.0000103870.31606.90.

46. Ravani P, Spergel LM, Asif A, Roy-Chaudhury P, Besarab A. Clinical epidemiology of arteriovenous fistula in 2007. *Journal of Nephrology* 2007; **20**(2): 141–149.

47. Kroll MH, Hellums JD, McIntire L V, Schafer AI, Moake JL. Platelets and shear stress. *Blood* 1996; **88**(5): 1525–1541.

48. Van Tricht I, De Wachter D, Tordoir J, Verdonck P. Hemodynamics and complications encountered with arteriovenous fistulas and grafts as vascular access for hemodialysis: A review. In *Annals of Biomedical Engineering*, vol 33, 2005; 1142–1157. DOI: 10.1007/s10439-005-5367-X.

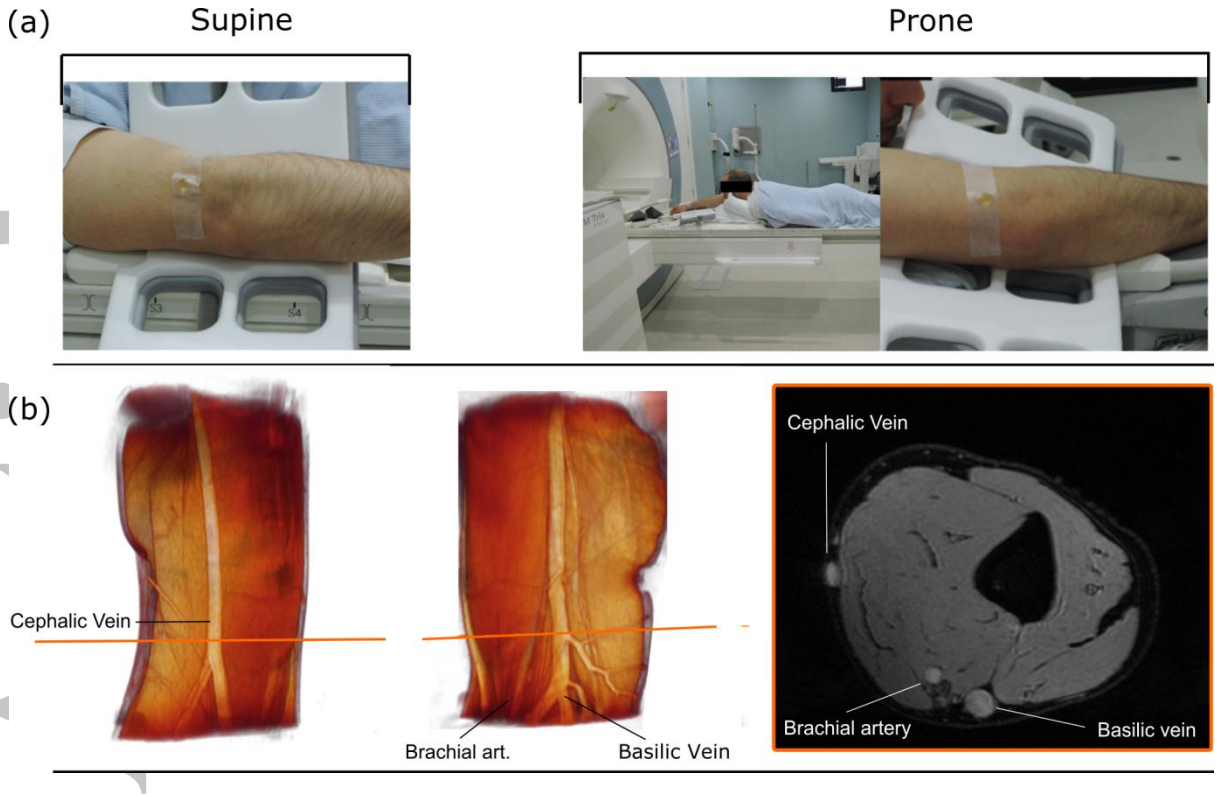

Figure 1: A volume render of the MEDIC DICOM data is shown in (a) along with an example of an Image slice. The fat suppression of the sequence allows for superficial vessels to be identified with ease. The position of a participant and surface coil is shown in (b) for the supine and prone positions respectively.

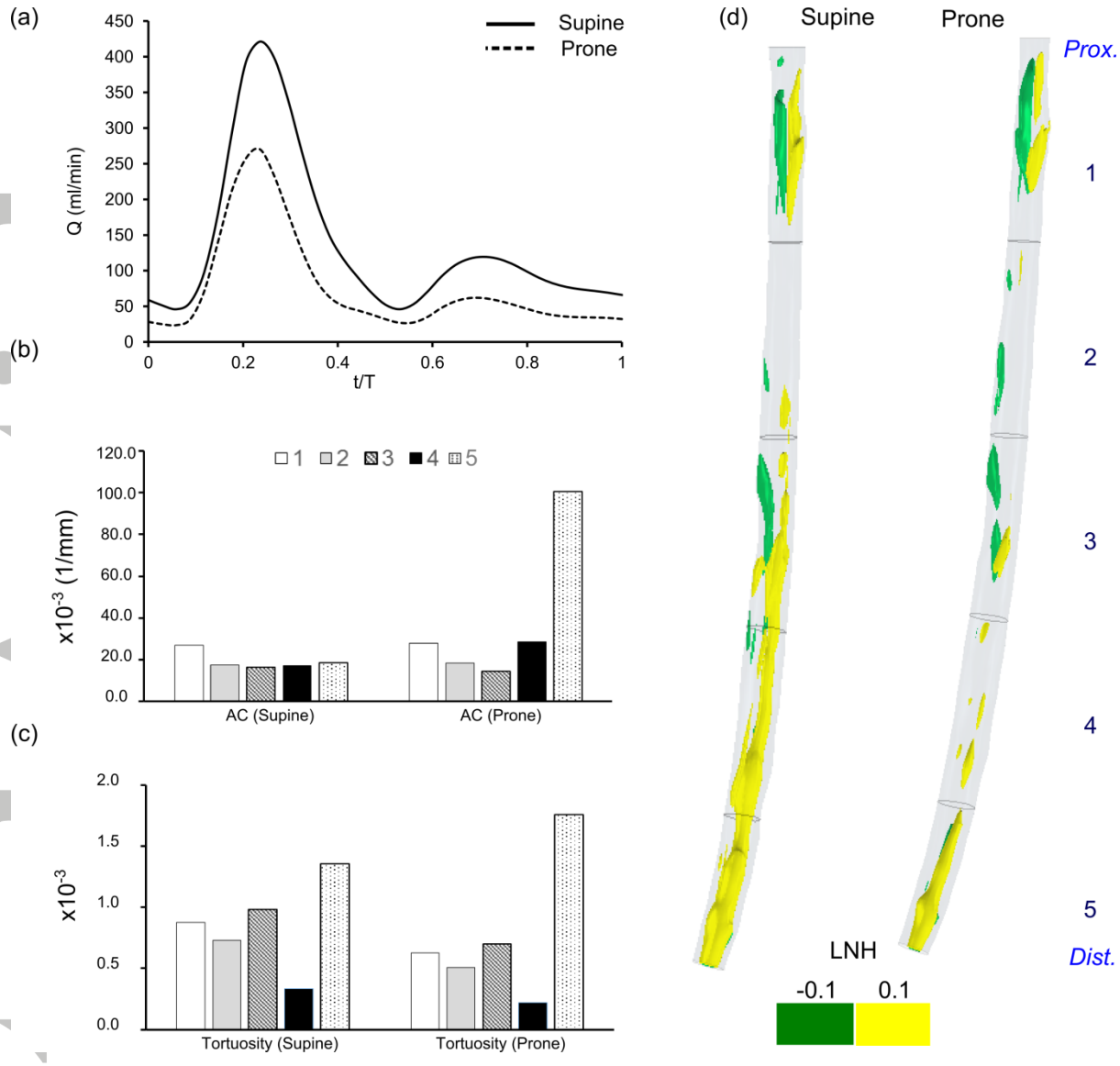

Figure 2: Flow waveform of the brachial artery of case 1 in the supine and prone position are shown in (a) Aggregated curvature and tortuosity measures are parented in (b) and (c). Isosurfaces of LNH visualising the low magnitude helical content of the bulk flow is presented in (d).

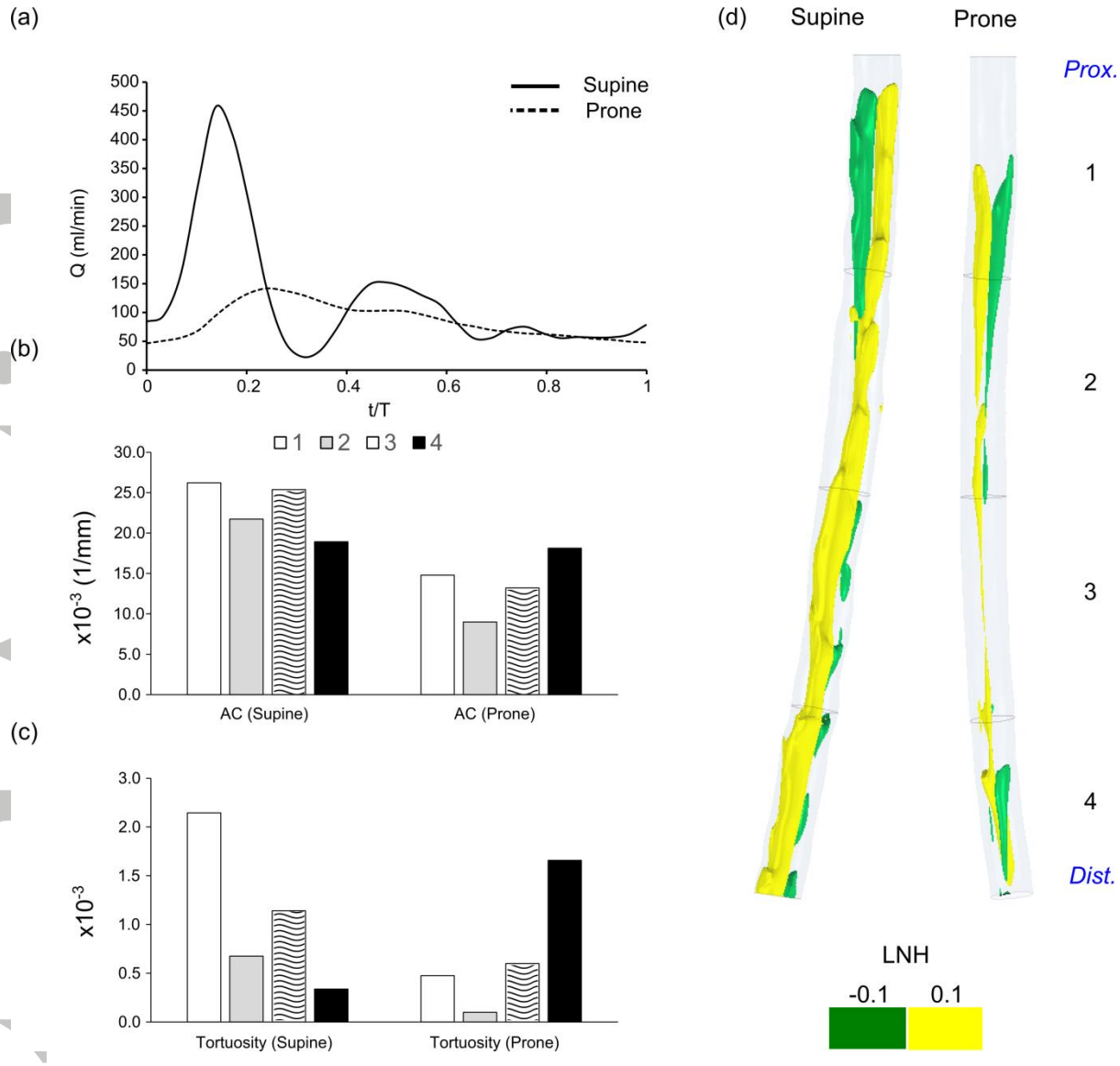

Figure 3: Flow waveform of the brachial artery of case 2 in the supine and prone position are shown in (a) Aggregated curvature and tortuosity measures are parented in (b) and (c). Isosurfaces of LNH visualising the low magnitude helical content of the bulk flow is presented in (d).

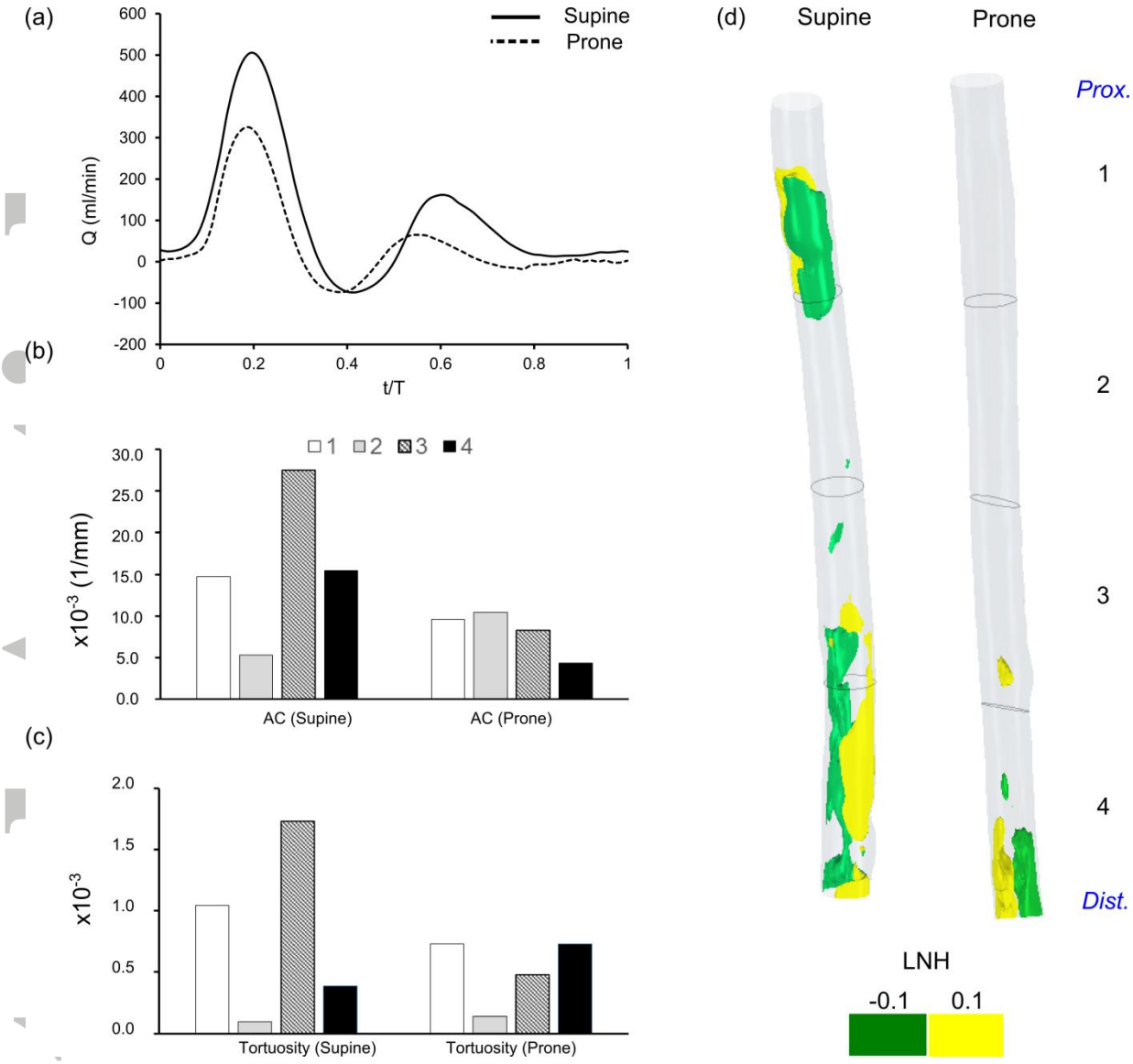

Figure 4: Flow waveform of the brachial artery of case 3 in the supine and prone position are shown in (a) Aggregated curvature and tortuosity measures are parented in (b) and (c). Isosurfaces of LNH visualising the low magnitude helical content of the bulk flow are presented in (d).

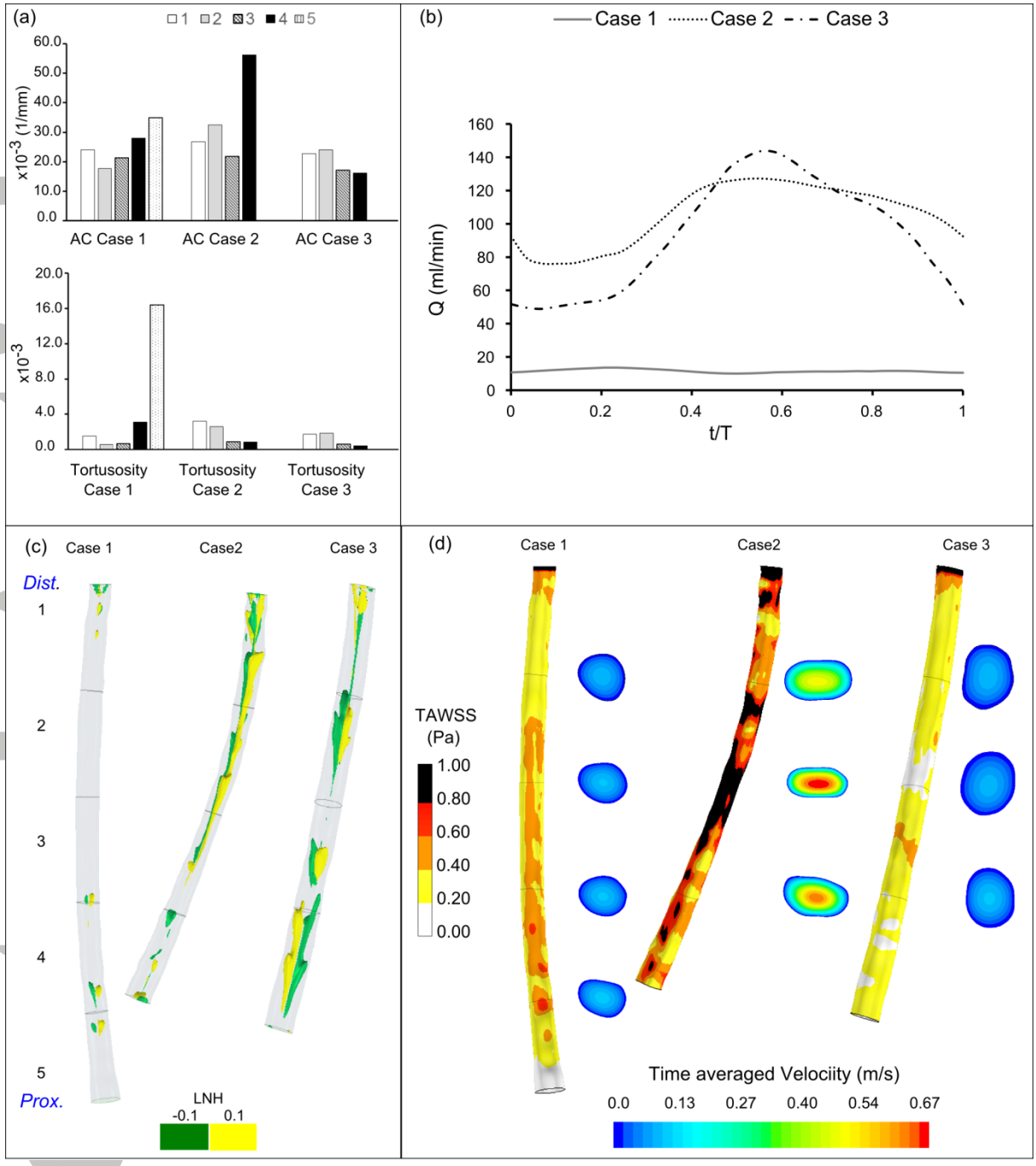

Figure 5: The curvature and tortuosity of the cephalic vein in the supine position for each case is show in (a) The inlet flow rate is presented in (b) The localised normalized helicity is shown in C and the time averaged wall shear stress and time averaged velocity for each cross section at 20 mm along the abscissa is shown in (d).

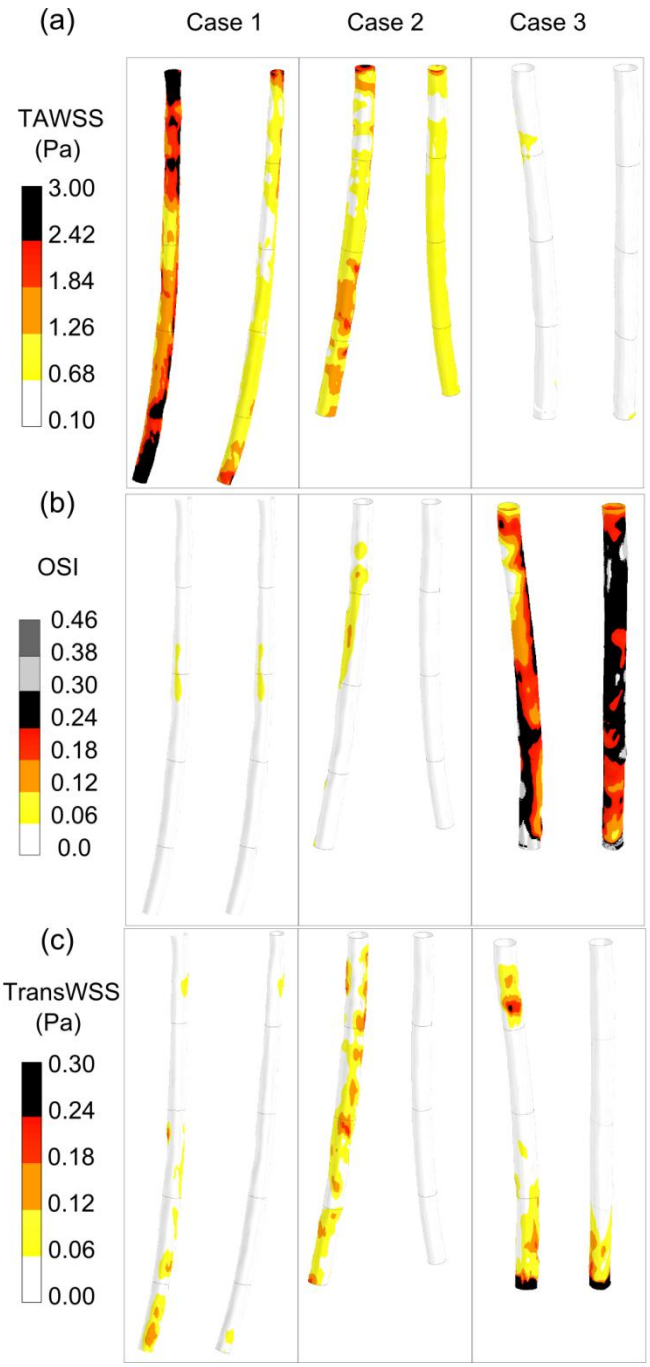

Figure 6: Time averaged wall shear stress, Oscillatory shear index and transverse wall shear stress are presented for the brachial artery in the supine and prone positions for each case. The prominent flow reversal in case 3 results in high values of OSI and lower shear stress levels compared to the other two cases.

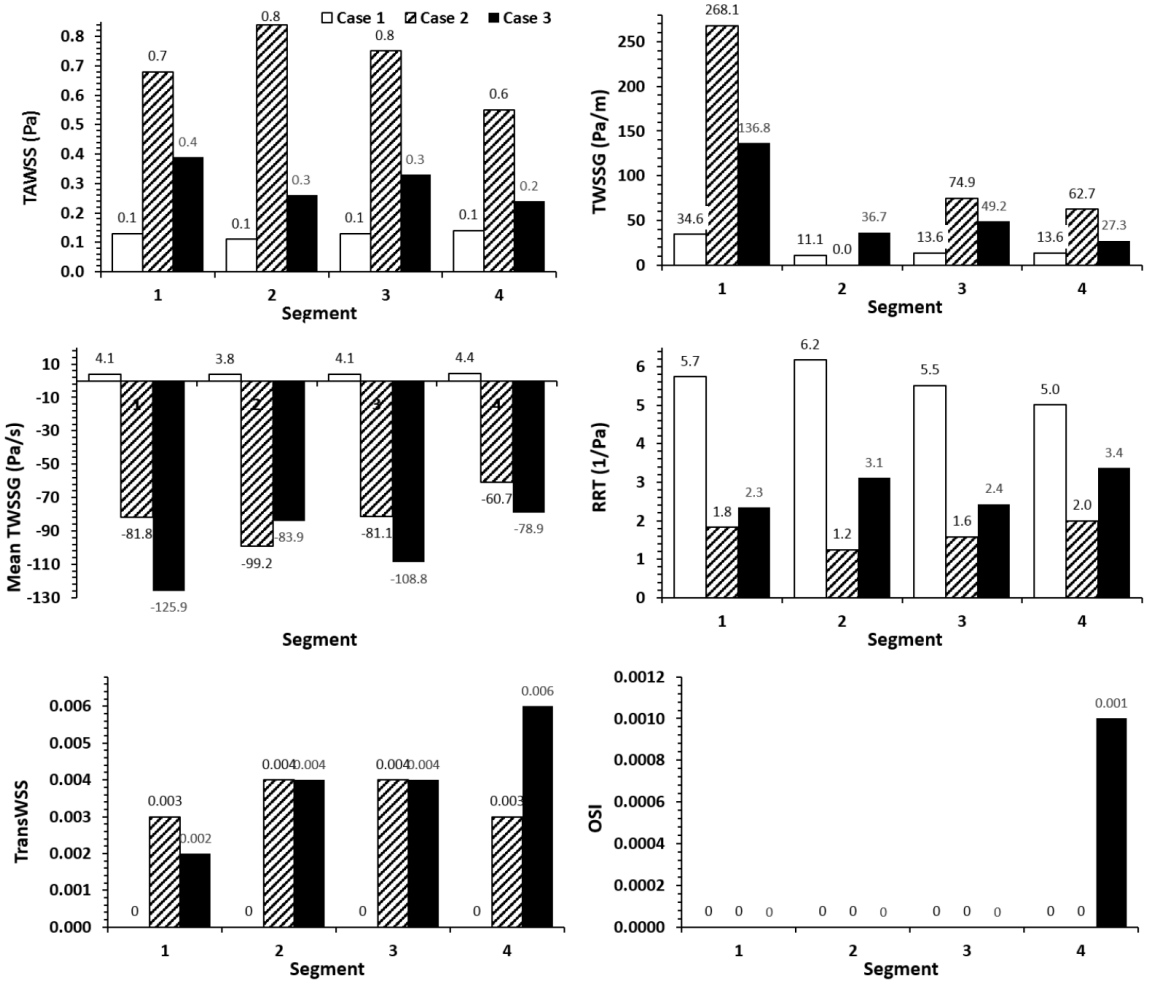

Figure 7: Surface averaged wall shear stress metrics for the cephalic vein for cases1, 2 and 3 in the supine position.

Table 1: Sequence acquisition parameters for MEDIC and 2D PCMRI to acquire vasculature and blood flow rates of the upper arm vasculatures**.**

	Units	**MEDIC**	**Arterial**	**Venous**
VENC	cm/s	-	75	15
TR	ms	29	61.7	61.7
TE	ms	16	5.88	5.88
Flip angle	°	8	30	30
Number of averages	-	1	3	3
Voxel size	mm	0.5 x 0.5 x 1.1	0.8 x 0.8 x 3.0	0.8 x 0.8 x 3.0
Slice thickness	mm	1.06	3	3
Base resolution	-	256	-	-
Phase resolution	%	100	-	-
Pixel bandwidth	Hz	161	260	260
Percentage Sampling	%	100	100	100
Percentage phase Field of view	%	100	75	75
Percentage phase Field of view	%	-	75	75
Number of time points	-	-	30	30
Acquisition time	min	5:17	1:52	1:35

Table 2: Discretisation error of the TAWSS over the vascular surface.

	Φ=TAWSS
N_1, N_2, N_3	176064, 595840, 1997458
r_{21}	1.501
r_{32}	1.497
Φ_1	4.717
Φ_2	4.716
Φ_3	4.715
P	2.432
ϕ_{ext}^{21}	4.718
e_a^{21}	0.01%
e_{ext}^{21}	0.01%
GCI_{fine}^{21}	0.01%

Table 3: Definitions of disturbed flow parameters and measures of helcial flow. Note: $\vec{\tau}_w$ represents the instantaneous WSS vector, t the time and T the period of the cardiac cycle.

Parameter	Abbreviation	Definition
Time average wall shear stress	TAWSS	$\frac{1}{T}\int_0^T \lvert\vec{\tau}_w\rvert dt$
Oscillating shear index	OSI	$0.5\left(1-\frac{\int_0^T \vec{\tau}_w\, dt}{\int_0^T \lvert\vec{\tau}_w\rvert dt}\right)$
Relative Residence Time	RRT	$\frac{1}{(1-2\times OSI)\ \times TAWSS}$
Transverse Wall Shear Stress	TransWSS	$\frac{1}{T}\int_0^T \left\lvert \vec{\tau}_w \cdot \left(\vec{n}\ \times \frac{\int_0^T \vec{\tau}_w\, dt}{\left\lvert\int_0^T \vec{\tau}_w\ dt\right\rvert}\right)\right\rvert dt$
Wall shear stress Gradient	TAWSSG	$\frac{1}{T}\int_0^T \sqrt{(\frac{d\vec{\tau}_w}{dx})^2+(\frac{d\vec{\tau}_w}{dy})^2+(\frac{d\vec{\tau}_w}{dz})^2}\ dt$
Temporal wall shear stress gradient	TWSSG	$\frac{1}{T}\int_0^T \left(\frac{d\vec{\tau}_w}{dt}\right) dt$
Helicity Density	H_k	$v(x,t)\cdot w(x,t)$
Localised Normalised Helicity	LNH	$\frac{v(x,t)\cdot w(x,t)}{\lvert v(x,t)\rvert\lvert w(x,t)\rvert}$

Table 4: Mean and peak blood flow rates of the brachial artery and cephalic vein are presented for each case. Mean (± SD) values amongst the subjects are also presented.

Case#	Brachial Artery (S) Flow Rate (ml/min)		Brachial Artery (P) Flow Rate (ml/min)		Cephalic Vein (S) Flow Rate (ml/min)	
	Mean	Peak	Mean	Peak	Mean	Peak
1	135.6	421.2	75.6	270.2	11.5	13.6
2	123.6	456.5	85.0	141.9	105.1	127.3
3	100.8	504.6	41.8	325.2	92.6	143.7
Mean ± SD	120.1±14.5	67.5±18.5	460.8±34.2	245.8±34.2	69.5±41.3	94.8±57.5

Table 5: Mean values (± SD) of curvature and tortuously of the brachial artery in the supine and prone position are presented with corresponding p values to determine any significant difference between the positions. Mean (± SD) values for curvature and tortuosity are also presented for the cephalic vein in the supine position.

	Brachial Artery			**Cephalic Vein**
	Supine	*Prone*	*P-value*	*Supine*
Curvature (1/mm)	0.014 ± 0.002	0.016 ± 0.006	0.38	0.026 ± 0.004
Tortuosity	0.006 ± 0.007	0.007 ± 0.007	0.26	0.007 ± 0.002

Table 6: Surface averaged wall shear stress metrics for the brachial artery for the supine (S) and prone (P) positions of case 1, 2 and 3, respectively.

	Segment	TAWSS (Pa)		TAWSSG (Pa/m)		TransWSS (Pa)		OSI (-)		RRT (1/Pa)		Mean TWSSG (Pa/s)	
		S	P	S	P	S	P	S	P	S	P	S	P
Case 1	1	2.83	1.25	401.05	181.10	0.03	0.03	0.00	0.01	0.39	0.92	619.96	303.46
	2	1.90	0.96	160.82	82.57	0.03	0.02	0.01	0.03	0.57	1.10	413.26	197.74
	3	1.89	0.96	262.28	121.09	0.05	0.02	0.01	0.02	0.60	1.07	363.17	237.02
	4	2.10	0.97	287.68	154.08	0.04	0.02	0.01	0.01	0.52	1.04	435.83	268.02
	5	2.85	1.38	601.23	306.94	0.06	0.03	0.00	0.00	0.39	0.76	642.28	407.11
Case 2	1	1.20	0.78	236.07	82.94	0.09	0.01	0.02	0.00	0.97	1.29	461.90	84.05
	2	1.01	0.81	147.26	47.70	0.06	0.01	0.03	0.00	1.07	1.20	356.01	95.28
	3	1.31	0.88	212.27	57.52	0.07	0.01	0.02	0.00	0.82	1.11	522.70	100.91
	4	1.09	0.91	226.26	86.61	0.07	0.01	0.03	0.00	1.02	1.08	369.75	102.82
Case 3	1	0.43	0.20	144.83	76.05	0.07	0.01	0.16	0.28	2.02	4.68	-197.15	-353.68
	2	0.44	0.24	117.19	71.36	0.03	0.02	0.19	0.27	1.77	3.65	-353.79	-393.62
	3	0.38	0.22	104.92	98.15	0.04	0.03	0.22	0.28	2.03	4.35	-474.70	-404.78
	4	0.43	0.31	126.78	329.59	0.14	0.16	0.21	0.26	2.46	3.82	-585.43	-555.82